JGR Earth Surface

RESEARCH ARTICLE
10.1029/2026JF009250

Coseismic Shallow Landslide Distributions Reveal Patterns of Regolith Thickness in High Mountains

Suryodoy Ghoshal[1], Sarah J. Boulton[1], Tristram C. Hales[2], Georgina Bennett[3], Amy Beswick[1], Joshua N. Jones[4], Shaun Lewin[1], Zoë K. Mildon[1], Martin Stokes[1], Michael R. Z. Whitworth[4], and Benjamin Campforts[5]

[1]Centre for Research in Natural Hazards and Risk Reduction, University of Plymouth, Plymouth, UK, [2]School of Earth and Environmental Sciences, Cardiff University, Cardiff, UK, [3]Department of Geography, University of Exeter, Exeter, UK, [4]Ground Engineering, AECOM, Plymouth, UK, [5]Department of Earth Sciences, Vrije Universiteit Amsterdam, Amsterdam, The Netherlands

Abstract Earthquake-triggered landslides are a major source of sediment mobilization in steep mountain landscapes, yet the controls that organize regional patterns of coseismic shallow failure remain incompletely understood. Because shallow landslides occur within regolith, their initiation and magnitude depend strongly on near-surface material thickness, which is rarely measured directly in mountainous terrain. Here we introduce *ShallowLandslider*, a hybrid physical–statistical framework that combines critical-acceleration slope-stability calculations with stochastic realization of discrete landslide populations. We apply the model to two geomorphically distinct subregions affected by the 2015 M_w 7.8 Gorkha earthquake in Nepal and compare modeled and observed distributions of landslide area, elevation, slope, and aspect. Parameterizations incorporating spatially variable regolith thickness consistently outperform a uniform-thickness baseline, and model performance is highest for moderate cohesion values ($c' \approx$ 10–15 kPa), characteristic of shallow colluvium. The two subregions favor contrasting regolith-organization hypotheses. In the high-relief, bedrock-dominated terrain of Subregion 1, landslide occurrence is reproduced most successfully by parameterizations that impose broad elevation-dependent thinning of regolith while landslide magnitude frequencies are best represented through a curvature-informed representation. In the lower-relief, more extensively regolith-mantled terrain of Subregion 2, curvature-informed parameterizations that represent local topographic convergence provide the closest agreement with the mapped inventory. These results indicate that landscape-scale organization of regolith thickness exerts a strong influence on coseismic shallow-landslide populations within the tested model framework. More broadly, they demonstrate how landslide inventories can be used to evaluate competing hypotheses of regolith distribution where direct observations remain sparse.

Plain Language Summary Large earthquakes can trigger thousands of landslides, moving regolith (the loose soil and weathered rock that mantles hillslopes) into rivers and valleys. Predicting where these landslides occur is difficult because regolith thickness varies across mountain landscapes and is rarely measured directly. We developed a new model, ShallowLandslider, that combines slope-stability physics with statistical methods to simulate populations of earthquake-triggered shallow landslides. We tested the model in two regions affected by the 2015 Gorkha earthquake in Nepal and compared simulated landslides with a mapped inventory. The model performed best when it included spatial variations in regolith thickness. In the steep, high-relief landscape, landslide occurrence was reproduced most successfully when regolith thickness decreased with elevation. In the lower-relief landscape, the best results occurred when thicker regolith was concentrated in convergent hollows where sediment accumulates. The simulations also matched observations most closely for cohesion values typical of shallow colluvium, supporting the interpretation that most Gorkha landslides were shallow, regolith-sourced failures. These results show that coseismic landslide patterns depend not only on ground shaking and slope steepness, but also on how regolith is organized across the landscape. Landslide inventories can help evaluate competing hypotheses of regolith distribution where direct observations are sparse.

Key Points:

- Representing spatial variability in regolith thickness substantially improves reproduction of coseismic shallow-landslide populations
- Gorkha landslide populations are reproduced most successfully for moderate effective cohesion values of 10–15 kPa
- High-relief terrain favors elevation-dependent regolith thinning, soil-mantled hillslopes favor curvature-informed thickening

Supporting Information:

Supporting Information may be found in the online version of this article.

Correspondence to:

S. Ghoshal,
suryodoy.ghoshal@plymouth.ac.uk

Citation:

Ghoshal, S., Boulton, S. J., Hales, T. C., Bennett, G., Beswick, A., Jones, J. N., et al. (2026). Coseismic shallow landslide distributions reveal patterns of regolith thickness in high mountains. *Journal of Geophysical Research: Earth Surface*, *131*, e2026JF009250. https://doi.org/10.1029/2026JF009250

Received 7 MAR 2026
Accepted 29 SEP 2026

Author Contributions:

Conceptualization: Suryodoy Ghoshal, Sarah J. Boulton, Tristram C. Hales, Benjamin Campforts
Data curation: Suryodoy Ghoshal, Amy Beswick, Shaun Lewin, Martin Stokes, Benjamin Campforts
Formal analysis: Suryodoy Ghoshal, Sarah J. Boulton, Tristram C. Hales, Georgina Bennett, Benjamin Campforts
Funding acquisition: Sarah J. Boulton

© 2026 The Author(s). Journal of Geophysical Research: Earth Surface published by Wiley Periodicals LLC on behalf of American Geophysical Union. This is an open access article under the terms of the Creative Commons Attribution License, which permits use, distribution and reproduction in any medium, provided the original work is properly cited.

1. Introduction

Major earthquakes commonly trigger thousands of landslides across mountainous terrain, (re)mobilizing regolith and rock over spatial extents of tens to hundreds of square kilometers. Coseismic landslides constitute a major

Investigation: Suryodoy Ghoshal, Sarah J. Boulton, Tristram C. Hales, Georgina Bennett, Amy Beswick, Joshua N. Jones, Zoë K. Mildon, Martin Stokes, Michael R. Z. Whitworth
Methodology: Suryodoy Ghoshal, Sarah J. Boulton, Tristram C. Hales, Georgina Bennett, Benjamin Campforts
Project administration: Suryodoy Ghoshal, Sarah J. Boulton
Resources: Sarah J. Boulton, Martin Stokes
Software: Suryodoy Ghoshal, Sarah J. Boulton, Tristram C. Hales, Shaun Lewin, Zoë K. Mildon, Benjamin Campforts
Supervision: Sarah J. Boulton, Tristram C. Hales, Zoë K. Mildon, Martin Stokes, Benjamin Campforts
Validation: Suryodoy Ghoshal, Sarah J. Boulton, Tristram C. Hales, Georgina Bennett, Martin Stokes, Benjamin Campforts
Visualization: Suryodoy Ghoshal, Tristram C. Hales, Amy Beswick, Joshua N. Jones, Shaun Lewin, Zoë K. Mildon, Michael R. Z. Whitworth, Benjamin Campforts
Writing – original draft: Suryodoy Ghoshal, Sarah J. Boulton, Tristram C. Hales, Georgina Bennett, Amy Beswick, Joshua N. Jones, Shaun Lewin, Zoë K. Mildon, Martin Stokes, Michael R. Z. Whitworth, Benjamin Campforts
Writing – review & editing: Suryodoy Ghoshal, Sarah J. Boulton, Tristram C. Hales, Georgina Bennett, Amy Beswick, Joshua N. Jones, Shaun Lewin, Zoë K. Mildon, Martin Stokes, Michael R. Z. Whitworth, Benjamin Campforts

secondary hazard, frequently disrupting infrastructure, damming rivers, and causing loss of life and economic damage that can sometimes rival the initial impacts of the earthquake itself (Fan et al., 2019; Petley, 2012). Beyond their immediate societal consequences, coseismic landslides exert a first-order control on sediment flux and topographic change in high mountain landscapes: they erode bedrock, rapidly transfer sediment from hillslopes to channels, and perturb drainage networks and post-seismic erosion patterns (Campforts et al., 2022; Hovius et al., 2011; Wang et al., 2020). Observations from recent earthquakes show that landslide occurrence is strongly organized by ground-motion intensity and topography, with higher densities generally occurring in areas of strong shaking, steep slopes, and high local relief (Kritikos et al., 2015; Parker et al., 2015; Roback et al., 2018). However, substantial variability often remains even within areas experiencing similar levels of shaking, suggesting that near-surface landscape properties also play an important role in organizing coseismic landslide populations. Understanding the physical controls on where coseismic landslides occur, and how their characteristics vary across landscapes, is therefore central to both regional hazard assessment and the feedbacks between tectonics, climate, and surface processes.

The size and triggering location of shallow landslides are strongly dependent on the spatial distribution of regolith throughout the landscape (D'Odorico & Fagherazzi, 2003; Claessens et al., 2007). The stability of that regolith depends on the interaction between regolith thickness and the additional strength provided by soil cohesion, root reinforcement, and overburden stresses (Milledge et al., 2014; Parker et al., 2016). Regolith commonly accumulates within convergent hollows and bedrock depressions, where sediment transport pathways concentrate material and promote the development of deeper colluvial stores that are particularly susceptible to shallow landsliding (Crozier et al., 1990; D'Odorico & Fagherazzi, 2003). As direct observations of regolith thickness are rare, shallow-landslide models typically either apply spatially uniform regolith thicknesses (Dietrich et al., 1995; Montgomery & Dietrich, 1994) or rely on empirical and modeled estimates (Pack et al., 1998; Segoni et al., 2012), with these choices often representing a major source of uncertainty in model predictions. Estimating regolith thickness is further complicated by the transition from continuously soil-mantled hillslopes to patchy regolith cover and ultimately bedrock-dominated terrain as relief increases and the balance between regolith production and erosion shifts (Heimsath et al., 2012; Rossi et al., 2026). In landscapes where a continuous regolith mantle is maintained, depth-dependent sediment transport can often be approximated as a linear or non-linear diffusive process, linking regolith thickness to topographic curvature (Roering, 2008). However, as soils thin and become discontinuous, the relationships between topography, regolith production, erosion, and rock strength become less clear, and curvature-based descriptions of regolith thickness may no longer be sufficient (Geyman et al., 2025; Heimsath et al., 2012; Rossi et al., 2026). Shallow landsliding nevertheless remains an important erosional mechanism in these thinly mantled landscapes (DiBiase et al., 2010). By definition, shallow landslides can only occur where regolith is present, raising the possibility that comprehensive shallow-landslide inventories can be used to evaluate competing hypotheses for how regolith thickness varies with topography in mountainous landscapes where direct observations are sparse.

Slope-stability models used to evaluate shallow landslide occurrence commonly rely on estimates of regolith thickness as a key controlling parameter (Claessens et al., 2007; Montgomery & Dietrich, 1994; Wong & Ho, 2000). Conversely, where landslide occurrence is known, physically based slope-stability models can be used to evaluate alternative hypotheses for how regolith thickness may vary across a landscape. In rainfall-triggered settings, models such as SINMAP (Pack et al., 1998) and SHALSTAB (Dietrich et al., 1995) combine infinite-slope stability theory with simplified hydrologic forcing to evaluate landslide susceptibility. More recently, multidimensional formulations have incorporated lateral support and explicit delineation of landslide geometry, allowing models to predict not only where instability occurs, but also the size and shape of individual failures (Bellugi et al., 2015; Milledge et al., 2014). Equivalent frameworks for coseismic shallow landsliding remain comparatively rare (Huang et al., 2020; Segoni et al., 2012), despite substantial uncertainty surrounding regolith thickness, material strength, and local shaking conditions. As a result, relatively few models provide a means of testing how alternative representations of regolith architecture influence the characteristics of coseismic landslide populations.

In this study, we introduce a new hybrid physical–statistical framework, *ShallowLandslider*, to test how alternative hypotheses for regolith-thickness organization influence the population-level characteristics of coseismic shallow landslides. The model couples a critical-acceleration stability calculation with stochastic realization of discrete landslide patches, bridging the gap between deterministic slope-stability modeling and probabilistic representations of landscape heterogeneity. We emphasize that the model is not evaluated here as a pixel-scale

predictor of individual landslide locations. Instead, we assess whether modeled landslide populations reproduce the observed distributions of landslide area, elevation, slope, and aspect, and therefore occupy similar topographic and geomorphic settings to the mapped inventory. By comparing modeled and observed landslide populations, we evaluate which topographically based hypotheses for regolith organization are most consistent with the mapped inventory and how those hypotheses influence patterns of coseismic landslide triggering. This framing allows us to ask which forms of regolith architecture best explain the observed organization of landslide populations in two contrasting Himalayan landscapes, while recognizing that unresolved ground-motion variability, site effects, material heterogeneity, and inventory uncertainty may also contribute to the observed patterns.

2. Methods

2.1. Study Area

The 2015 M_w 7.8 Gorkha earthquake in Nepal provides a compelling natural laboratory for (a) evaluating the performance of *ShallowLandslider* and (b) testing alternative hypotheses for how regolith thickness is organized across mountainous topography. The event ruptured a ∼150 km segment of the Main Himalayan thrust between the Gorkha region northwest of Kathmandu to the Ramechhap region in eastern-central Nepal (Avouac et al., 2015; USGS, 2015), producing peak ground accelerations (PGA) locally exceeding 0.6g, and triggering widespread slope failures across an area of more than 30,000 km^2. Over 25,000 landslides were mapped in its aftermath by a succession of groups around the world (Figure 1), making it one of the most comprehensively documented cases of coseismic landsliding worldwide (Kargel et al., 2015; Meena & Tavakkoli Piralilou, 2019; Roback et al., 2018). The failures were concentrated in areas of high PGA and rugged topography north of the Kathmandu valley, with fewer, smaller events occurring in the southern foothills (Roback et al., 2018). The broad spatial pattern of landsliding followed gradients in shaking intensity and local relief, offering a natural experiment for evaluating how modeled landslide populations vary across contrasting real-world topographic settings. The vast majority of these landslides were shallow, regolith-sourced failures rather than deep-seated bedrock landslides. This distinction is critical: shallow landslides are sensitive to both the spatial organization of regolith thickness and to moderate cohesion values typical of mobile regolith (Montgomery & Dietrich, 1994).

We evaluate *ShallowLandslider* in two subregions within the landslide-affected zone (Figures 1 and 2). These subregions were selected to isolate the influence of contrasting topography and regolith structure under similar shaking conditions, and together they represent complementary test cases for examining the transferability of regolith-depth parameterizations.

Subregion 1 (northwest of Kathmandu): This area lies immediately east of the earthquake epicenter and experienced some of the strongest shaking (PGA ≈ 0.6 g). Despite this, it produced a moderate number of landslides (n = 523; Figure 1). Elevations range from ∼1500–6,000 m (mean ≈ 3,800 m), with a relief of 4,626 m. Slopes vary almost normally between subhorizontal to ∼68° (mean = 37°). Failures mapped in this subregion were concentrated at the lower end of the regional elevation distribution, with very few failures above 4,000 m. Failures are largely concentrated at steeper slopes, with most occurring on slopes >35°−50° (Figure 2).

Subregion 2 (northeast of Kathmandu): This region follows the Araniko Highway toward the Nepal-China border and is highly landslide-prone, due to both monsoon rainfall and coseismic shaking. It was affected by both the mainshock and the M_w 7.3 aftershock, with PGA ≈ 0.6 g, triggering over 2,300 landslides (Figure 1). The average elevation here is considerably lower than in Subregion 1, ranging from 1,000 to 3,500 m (mean ≈ 2,500 m), with a relief of 2,712 m. The slope distribution is similar to Subregion 1, ranging between subhorizontal to ∼60°, but with a lower mean (26°). Landslides occur across the full elevation range but again tend to cluster on slopes steeper than 35°–50° (Figure 2). This area is also heavily modified by human activity, particularly along the Araniko corridor, where extensive road construction, slope cutting, and deforestation contribute to locally unstable slopes and increased regolith disturbance. These two landscapes differ strongly in hypsometry, degree of topographic convergence, and degree of vegetation cover, which reflects differences in the thickness of the soil mantle. This provides a natural test-bed for testing whether broad elevation trends or fine-scale curvature-driven regolith accumulation exerts greater control on shallow coseismic failure.

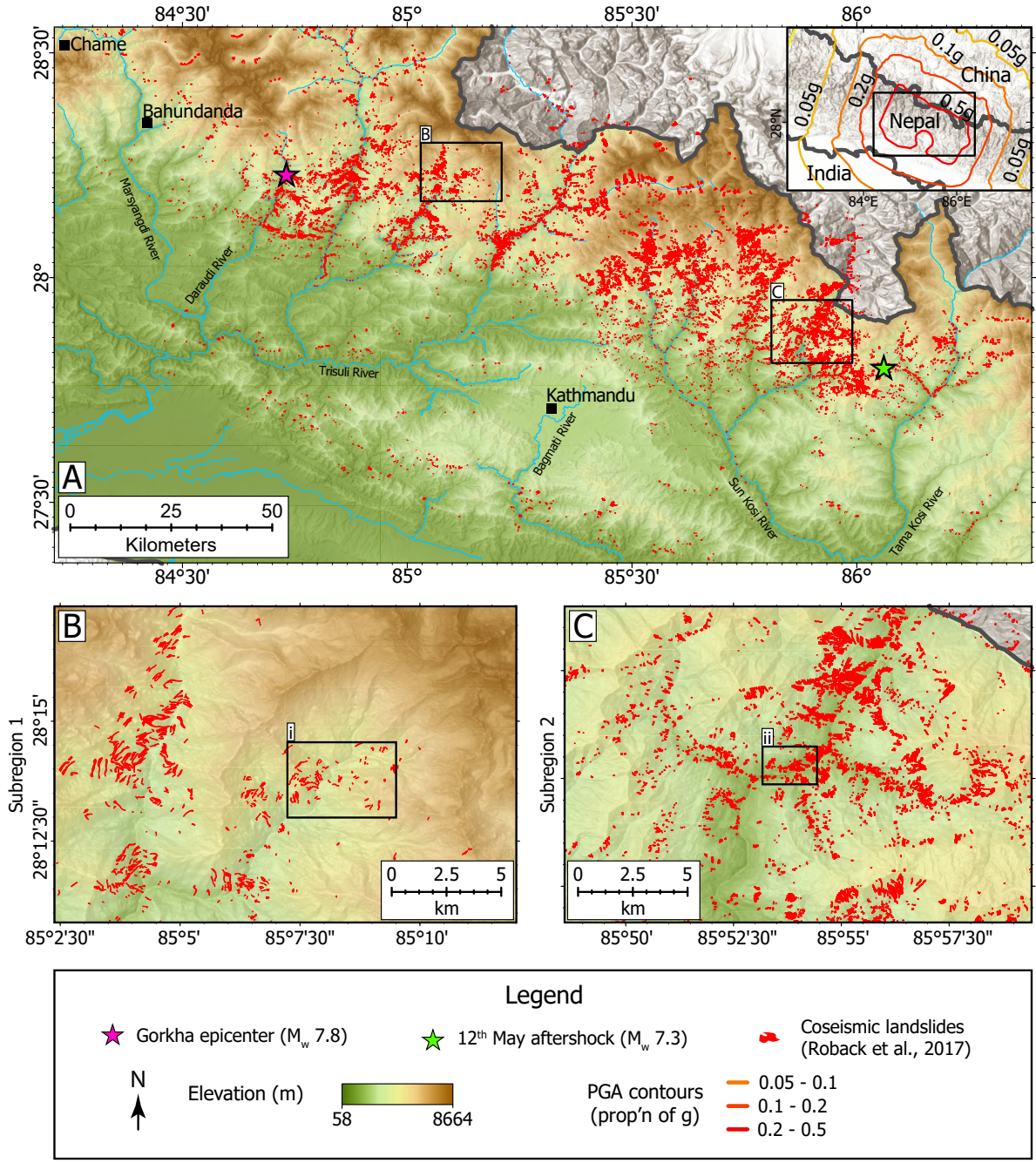


Figure 1. (a) Map of coseismic landslides (red) triggered by the 2015 M_w 7.8 Gorkha earthquake (Roback et al., 2018). The pink star marks the mainshock epicenter and the green star marks the M_w 7.3 aftershock of 12 May 2015. Contours in the inset show peak ground acceleration (proportion of g) from the USGS ShakeMap (USGS, 2015). (b) Topography and mapped landslides in Subregion 1, illustrating its high-relief, bedrock-dominated terrain. (c) Topography and mapped landslides in Subregion 2, which is characterized by lower relief and more extensive regolith mantling. Boxes (i) and (ii) show the locations of the images shown in Figure 2.

2.2. Physical Slope-Stability Model

ShallowLandslider evaluates coseismic slope stability using a three-dimensional critical-acceleration formulation derived from the Newmark sliding-block method. We use the Newmark framework to define the acceleration threshold required for mechanical instability, but we do not calculate or validate Newmark displacement. The seismic forcing is represented by gridded peak horizontal and vertical accelerations, so the model does not resolve shaking duration, frequency content, rupture directivity, or the full acceleration time history. The resulting

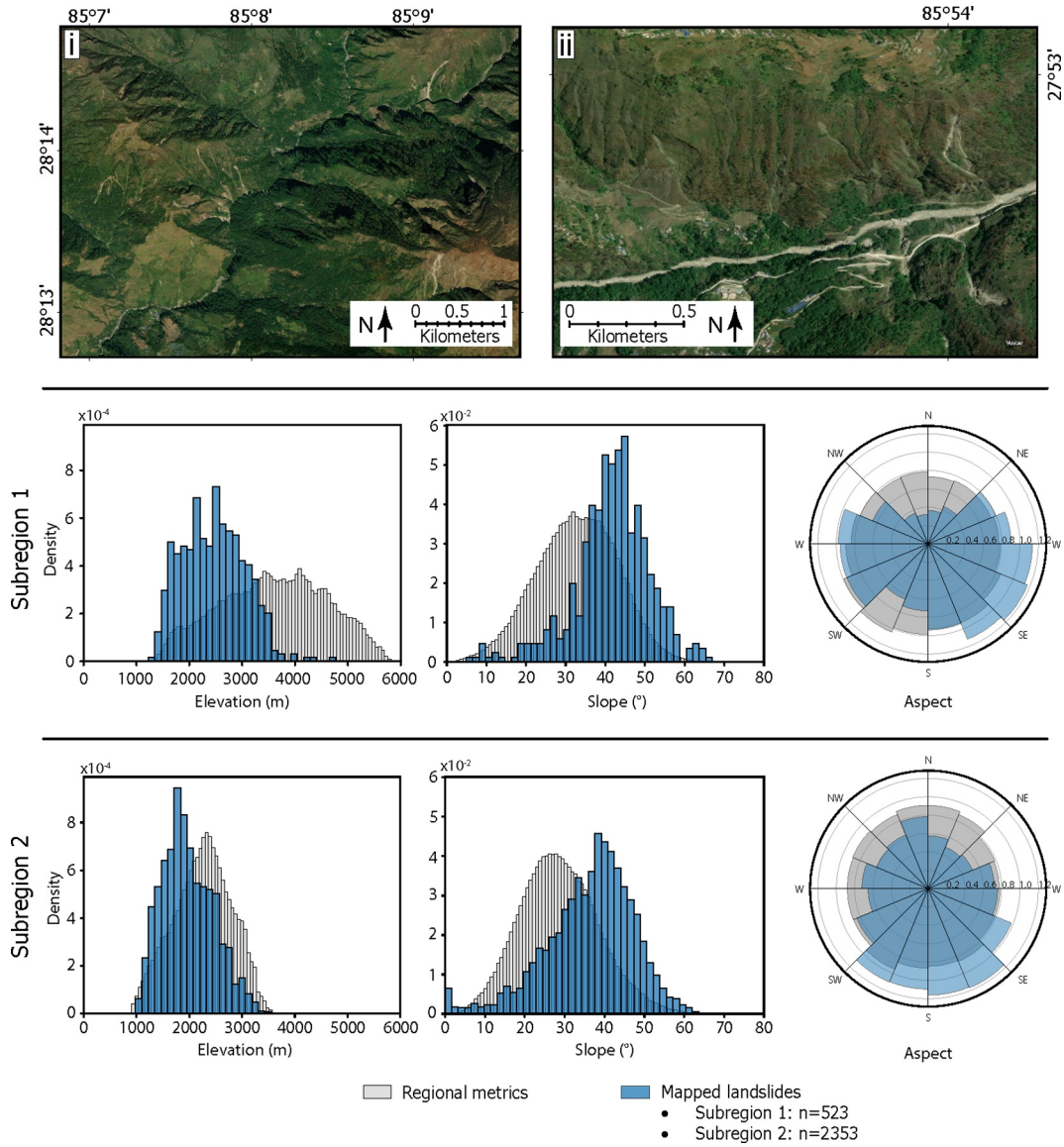


Figure 2. (i) Satellite image of a small part of Subregion 1 showing steep, highly dissected, bedrock-dominated topography. (ii) Satellite image of a small part of Subregion 2 showing rolling, regolith-mantled hillslopes with pervasive convergent hollows. Imagery source: Esri, Maxar, Earthstar Geographics, and the GIS User Community (acquired between 2018 and 2024). Histograms and rose diagrams show the density distributions for elevation and slope for the entire study subregions shown in Figures 1b and 1c. Gray bars show regional distribution, while blue bars show distribution for mapped subregional landslides.

instability field is therefore interpreted as a mechanically constrained candidate set for shallow failure, rather than as a prediction of displacement magnitude or final landslide motion.

The model computes mechanical instability at each grid node based on local slope angle, regolith thickness, material strength, and seismic accelerations, and stochastically samples the mechanically unstable terrain to select discrete landslides. In this subsection, we outline the governing equations and describe how they are incorporated into the model workflow. A schematic of the Newmark sliding-block geometry and the representation of regolith thickness and saturation is provided in Figure S1 of the Supporting Information S1. Figure 3 provides a broad overview of the modeling workflow, with Table 1 listing all parameters used in the model, their definitions, units, and any default values.

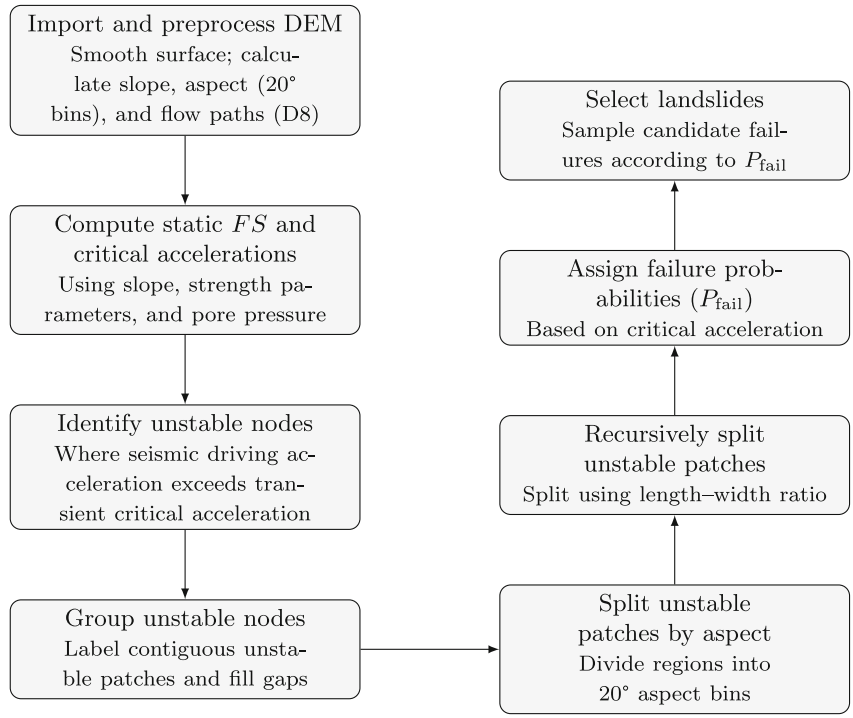


Figure 3. Workflow of *ShallowLandslider*, showing DEM preprocessing, factor-of-safety and critical-acceleration calculations, identification of unstable nodes, geometric grouping and subdivision of unstable patches, assignment of failure probabilities, and final selection of realized landslides.

2.2.1. Infinite-Slope and Newmark Formulation

The Newmark method conceptualizes landslide initiation as the downslope displacement of a rigid block sliding on an infinite slope. Failure occurs when the seismic driving acceleration (a_s) exceeds the critical acceleration (a_c), the threshold required to overcome resisting forces (Jibson et al., 2000; Newmark, 1965). The critical acceleration depends on the static factor of safety (FS) and slope angle (α):

$$a_c = (\text{FS} - 1) * g \sin \alpha \tag{1}$$

The static factor of safety for a saturated regolith layer of thickness h_s is given by (Jibson et al., 2000):

$$\text{FS} = \frac{c'}{\gamma_t h_s \sin \alpha} + \frac{\tan \phi'}{\tan \alpha} - \frac{m \gamma_w \tan \phi'}{\gamma_t \tan \alpha} \tag{2}$$

where, c' is the effective cohesion, ϕ' is the angle of friction, γ_t and γ_w are the unit weights of regolith (unsaturated) and water, respectively, and m is the proportion of submerged regolith (Figure S1 in Supporting Information S1).

Under dry or partially saturated conditions, pore-water pressure effects diminish and suction enhances shear strength. In this case, FS becomes:

$$\text{FS} = \frac{c' + (\sigma_n - u_a) \tan \phi' + (u_a - u_w) \tan \phi^b}{\gamma_t h_s \sin \alpha} \tag{3}$$

where σ_n is the total normal stress, $\sigma_n - u_a$ is the net normal stress on the slip surface, u_a and u_w are pore water and air pressure, respectively, $u_a - u_w \equiv \psi$ = matric suction, and ϕ^b = angle of increase in shear strength with matric suction (Cho & Lee, 2002; Huang et al., 2020). For low saturation, $\phi^b \approx \phi'$ (Wong & Ho, 2000).

Table 1
Notation and Symbols Used in ShallowLandslider

Symbol	Description	Default value (if any)
Geometric Parameters		
α	Slope angle (°)	–
h_s	Regolith thickness in normal direction (m)	–
m	Proportion of submerged regolith	0.5
Strength Parameters		
c'	Effective cohesion (Pa)	–
ϕ'	Effective angle of friction (°)	30
ϕ^b	Angle of increase in shear strength with matric suction (°)	–
FS	Static factor of safety	1.0
Unit Weight		
γ_t	Unit weight of regolith (kN m^{-3})	15
γ_w	Unit weight of water (kN m^{-3})	9.81
Stress and Pore Pressure (Pa)		
σ_n	Total normal stress	–
$\sigma_n - u_a$	Net normal stress on the slip surface	–
u_a	Pore air pressure	0
u_w	Pore water pressure	–
ψ	Matric suction $(u_a - u_w)$	–
u	Pore pressure replacement for ψ $(m\gamma_w h)$	–
Seismic Parameters (m s^{-2})		
g	Acceleration due to gravity	9.81
a_c	Critical acceleration	–
$a_{c,transient}$	Critical transient acceleration	–
a_s	Sliding acceleration	–
a_n	Acceleration normal to the slope	–
a_h, a_v	Horizontal/vertical acceleration (PGA)	–

Note. The table summarizes the geometric, mechanical, hydrologic, and seismic parameters used in the factor-of-safety and critical-acceleration calculations, along with their default values (if any). Additional symbols, parameters, and code-level variables associated with the regolith-thickness parameterizations are defined in Tables S1–S3 of the Supporting Information S1.

We can represent σ_n = weight × cos α, where the weight of the sliding block is the unit weight of the regolith multiplied by the thickness of the block (weight $= \gamma_t h_s$). Additionally, since matric suction (ψ) can be written as $(u_a - u_w)$, and $u_a = 0$, Equation 3 simplifies to:

$$\mathrm{FS} = \frac{c' - \psi \tan\phi'}{\gamma_t h_s \sin\alpha} + \frac{\tan\phi'}{\tan\alpha} \tag{4}$$

Substituting Equation 4 into Equation 1 yields the time-independent critical acceleration required to initiate sliding of the regolith layer:

$$a_{c,\mathrm{constant}} = \frac{c'g - \psi g \tan\phi'}{\gamma_t h_s} + g\cos\alpha\tan\phi' - g\sin\alpha \tag{5}$$

In this formulation, cohesion and regolith thickness jointly determine the depth and location of the potential failure plane, making the Newmark approach inherently sensitive to shallow, regolith-sourced failures. Variations in c' therefore act as a proxy for uncertainty in regolith fabric, root reinforcement, and unresolved near-surface strength heterogeneity, while variations in h_s directly alter the resisting mass and thus the likelihood of shallow failure. Groundwater effects are represented separately through the saturation term m and its associated pore-pressure contribution. While mechanical instability (i.e., FS $\leq$ 1) identifies terrain that is capable of failing under seismic loading, it does not by itself identify a realized landslide. For fully or partially saturated conditions (i.e., where the sliding plane is submerged), matric suction does not contribute additional shear resistance and can instead be represented through pore-water pressure effects. In this case, the suction term (ψ) may be replaced by the pore pressure $(u = m\gamma_w h_s)$. Throughout this study we assume a constant saturation state ($m = 0.5$; Table 1), while recognizing that groundwater conditions vary spatially across the landscape.

2.2.2. Transient Seismic Forcing

During an earthquake, both horizontal (a_h) and vertical (a_v) accelerations modify normal stress and driving forces. The acceleration normal to the slope is:

$$a_n = a_v(t)\cos\alpha + a_h(t)\sin\alpha \tag{6}$$

and the transient critical acceleration is (Huang et al., 2020):

$$a_{c,\mathrm{transient}}(t) = \left(\frac{c'g - gu\tan\phi'}{\gamma_t h_s}\right) - g\sin\alpha + \tan\phi'(g\cos\alpha - a_v(t)\cos\alpha - a_h(t)\sin\alpha) \tag{7}$$

The downslope driving acceleration $a_s(t)$ is defined as:

$$a_s(t) = a_h(t)\cos\alpha - a_v(t)\sin\alpha \tag{8}$$

A grid cell becomes a candidate for failure when $a_s(t) > a_{c,\mathrm{transient}}(t)$. In this study, we use spatially gridded horizontal and vertical PGA components and evaluate failure potential based on peak acceleration values. We do not integrate acceleration time histories or calculate Newmark displacement; the resulting output is therefore a critical-acceleration-based instability candidate set rather than a displacement prediction. The PGA fields are

derived from the USGS ShakeMap for the Gorkha earthquake (USGS, 2015) and therefore inherit uncertainties associated with spatial interpolation, site amplification, topographic effects, and rupture-related variability that are not explicitly represented in the model. Model results should therefore be interpreted in the context of these unresolved uncertainties in the seismic forcing field.

2.3. Model Framework and Implementation

ShallowLandslider organizes the slope-stability calculations described above into a modular workflow that progresses from DEM preprocessing to population-level landslide realization. Although the overall framework also includes a runout and mobility component, it is still in development. The present study focuses exclusively on the landslide-identification module, which delineates mechanically unstable terrain but does not simulate post-failure motion. In this section, we describe how the component implements these physics on a gridded landscape; how topographic attributes are calculated, how mechanically unstable terrain is grouped and partitioned into candidate slope units, and how landslides are ultimately selected through a probability-based sampler. Deterministic mechanical instability (i.e., FS $\leq$ 1) is a necessary but insufficient condition for a realized landslide. This workflow (Figure 3) is implemented within the Landlab framework and is designed to ensure that physically derived instability patterns are translated into realistic, spatially coherent landslide populations.

2.3.1. Topography and Spatial Discretization

We use a lightly smoothed 30 m SRTM DEM for each subregion as our gridded framework. To suppress pixel-scale artifacts and striping while preserving hillslope curvature, we apply a 3 $\times$ 3 median filter to the DEM prior to calculating any topographic parameters. However, it may also smooth narrow hollows, road cuts, and other features below the effective grid scale. The model should therefore be interpreted as resolving regional hillslope-scale patterns rather than very local failure controls. This smoothing is optional and would not be necessary for products such as NASADEM, or MERIT, which are preprocessed to mitigate these issues, or for grids that have been smoothed by erosive processes in broader landscape evolution modeling scenarios. The 30 m resolution DEM was selected due to its wide availability, and its balance between capturing hillslope-scale variability and computational efficiency. We computed slope, topographic aspect, and planform curvature at each grid node for use in stability calculations and regolith thickness parameterizations (Figure 3). Planform curvature was calculated using the RichDEM implementation of the Zevenbergen and Thorne (1987) method, which fits a quadratic surface to each grid cell and its neighbors and computes curvature perpendicular to the maximum slope direction. Flow routing uses D8 connectivity to obtain contributing drainage area where required.

2.3.2. Regolith Thickness Parameterization

We implemented five regolith-thickness parameterizations to evaluate how different geomorphic assumptions about colluvial storage influence the population-level organization of coseismic shallow landsliding. Each parameterization represents a distinct hypothesis about how regolith accumulates across steep Himalayan terrain rather than as a directly validated map of true regolith thickness. The aim is therefore to test how alternative representations of regolith architecture affect population-level landslide characteristics under the same stability formulation and ground-motion field. Expanded implementation details, equations, and parameter definitions for the regolith-thickness parameterizations are provided in Text S1 and Tables S1–S3 of the Supporting Information S1.

The simplest configuration applies a uniform, constant regolith depth of $h_s = 1\,\mathrm{m}$ across the DEM. Spatially uniform regolith thickness has been widely used in physically based slope-stability models where direct observations of regolith thickness are unavailable (Dietrich et al., 1995; Montgomery & Dietrich, 1994). Here, it serves as a deliberately simple baseline against which the value of introducing spatial organization can be assessed. The configuration is not intended to represent a physically realistic regolith-thickness distribution in steep Himalayan terrain and necessarily ignores natural heterogeneity in regolith production, transport, and erosion. To incorporate broad-scale hypsometric structure, the inverse elevation-dependent parameterization imposes a linear decrease in regolith depth with height, from a maximum of $h_{s,\max} = 1.5\,\mathrm{m}$ in the lowest-elevation portions of the model domain to $h_{s,\min} = 0\,\mathrm{m}$ at the highest elevations. This design reflects well-documented patterns of regolith thinning on steep ridges, where enhanced erosion and reduced deposition limit colluvial accumulation (Dietrich

et al., 1995; Li et al., 2017; Pelletier & Rasmussen, 2009). The normalization and linear scaling used in the model are given in Text S1.1 of the Supporting Information S1.

A second class of parameterizations focuses on topographic convergence. In the drainage-area-dependent formulation, regolith thickness is scaled to the upstream contributing area derived from flow routing, such that nodes in hollows and valley floors acquire thicker colluvial packages, whereas divergent slopes and ridgelines remain thin. This approach reflects the geomorphic tendency for sediment to accumulate in convergent topography, linking regolith thickness directly to hillslope transport pathways and hydrologic connectivity (Catani et al., 2010; Dietrich et al., 1995; Park et al., 2001; Parker et al., 2016). More details about the implementation of this parameterization are provided in Text S1.4 and Table S3 of the Supporting Information S1.

Similarly, the curvature-dependent parameterization assigns regolith thickness as a function of planform curvature κ. Classical hillslope soil-production models (Dietrich et al., 1995, 2013; Heimsath et al., 1997) relate h_s to curvature through a non-linear logarithmic expression $\left(h_s(\kappa) = -h_* \ln \frac{D_\kappa}{P_0}\right)$, which captures the rapid thickening of regolith in concave hollows and its thinning on convex slopes. However, because the logarithmic term diverges for $\kappa \leq 0$, the formulation requires piecewise definitions and can be difficult to apply consistently across large, heterogeneous landscapes. Following Patton et al. (2018), we use a linear approximation, $h_{s,\kappa} = \bar{h} + \beta\kappa$, where $\bar{h}$ is the reference regolith thickness, κ is planform curvature, and β is a curvature–thickness coefficient derived from the local standard deviation of curvature, σ_κ. To avoid unrealistically thick or negative depths in strongly concave or convex areas, values are clipped to the range 0–1.5 m. Further details of the curvature formulation, including the definition of σ_κ, the local-window calculation, and the depth clipping procedure, are provided in Text S1.2 and Table S2 of the Supporting Information S1.

Finally, to combine large-scale hypsometric control with fine-scale topographic variability, we constructed an elevation-weighted curvature parameterization in which regolith thickness is computed as the mean of the elevation-dependent estimate $h_{s,\text{elev}}$ and the curvature-derived value $h_{s,\kappa}$. This hybrid formulation imposes gradual thinning of regolith toward high ridges while incorporating the local effects of hillslope convergence and divergence. As with the other parameterizations, depths are clipped to 0–1.5 m to maintain physical plausibility. The calculation of the elevation-weighted curvature field is provided in Text S1.3 of the Supporting Information S1.

2.3.3. Material Strength and Cohesion

Effective cohesion (c') and the angle of internal friction (ϕ') govern the shear resistance of the regolith in the infinite-slope formulation (Equations 2–7; Table 1). To isolate the interaction between regolith architecture and material strength, we vary c' systematically over a plausible shallow-regolith range (0–20 kPa) for each regolith-depth structure while holding other parameters fixed within representative regional values (Campforts et al., 2022; Huang et al., 2020). ϕ' is held constant at 30° to avoid covariance with c', ensuring that differences in modeled landslide populations arise primarily from the combined effects of regolith thickness (h_s) and cohesion. This design emphasizes the depth-sensitivity of shallow failures: lower cohesion values reduce shear resistance and promote failure in thinner regolith, whereas higher cohesion suppresses failure except in locally thicker or steeper terrain. Although we hold ϕ' constant, we note that varying the friction angle would primarily shift the range of slope angles susceptible to failure. All other mechanical parameters follow standard regional values (Table 1).

2.3.4. Simulating Landslide Populations

Mechanically unstable terrain identified from the critical-acceleration calculation often forms spatially extensive, connected patches when evaluated on DEM grids. These connected regions cannot be interpreted directly as individual landslides, because DEM connectivity may link multiple adjacent slope faces across ridges, channels, or broad unstable hillslope zones. We therefore apply a population-based geometrical partitioning to divide them into discrete candidate landslides, ensuring consistency with empirical distributions of landslide size and shape. This hybrid physical–statistical design targets population-level characteristics, such as landslide size distributions and topographic settings, rather than predicting the exact footprint of each mapped landslide. From the set of mechanically unstable nodes, we generate discrete landslides through two sequential steps: (a) geometric

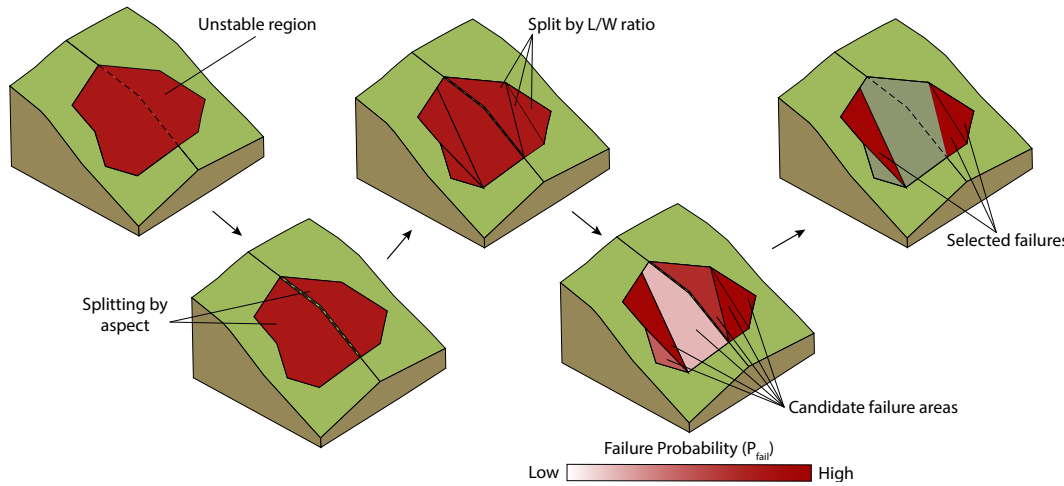


Figure 4. Schematic of the landslide-population selection workflow. Unstable nodes identified from the Newmark-based stability analysis are grouped into contiguous regions, subdivided by slope-aspect zones to isolate individual slope faces, and iteratively split using empirical length–width constraints. Each candidate patch is then assigned a failure probability based on its median a_c, and realized landslides are obtained through weighted stochastic sampling.

partitioning of unstable terrain into candidate failures, and (b) probabilistic sampling to reflect unresolved uncertainty in material properties and localized triggering (Figures 3 and 4):

1. Region splitting: Unstable nodes are first grouped into contiguous regions based on spatial connectivity. To reduce artificial connections across channels and ridgelines, each connected region is split into smaller patches based on topographic aspect bins of 20°, essentially isolating single slope faces. However, because of the discrete nature of the bins, neighboring cells may occasionally be separated despite small underlying aspect differences. The downslope length and cross-slope width of each resulting patch are then compared to the empirical length-width distribution of the mapped landslide inventory. Patches falling outside this distribution, either where width exceeds length, or where lengths are disproportionately large, are split at their centroid. This process is applied recursively: after each split, the dimensions of all subregions are recalculated, and those still falling outside the empirical range are split again, until at least 75% of areas conform to the observed length-width relationship. This procedure constrains modeled landslides to realistic slope-parallel geometries that are broadly consistent with shallow translational failures, while recognizing that some complex or composite landslides may be simplified by the partitioning process.
2. Stochastic sampling: While the static factor of safety of a slope can be readily calculated, the dynamic processes of triggering and the spatial and temporal variability in strength cannot be determined using the static Mohr-Coulomb method. Therefore, we introduce a stochastic sampling component, where each candidate region is assigned a failure probability $\left(P_{\text{fail}}\right)$ inversely proportional to its median critical acceleration. Therefore, regions with high critical acceleration (i.e., requiring a higher PGA to overcome the frictional forces) would have lower P_{fail}, and vice versa. The median critical acceleration is a robust measure of resistance that biases selection toward mechanically more failure-prone regions while preserving variability. A weighted sampler then selects a subset of candidate regions as landslides; the selection proportion reflects both the mean and spread of the probability field $\left(\overline{P_{\text{fail}}} + \sigma_{P_{\text{fail}}}\right)$, ensuring that the number of selected landslides reflects both central tendency and variability in P_{fail}. This approach introduces some stochasticity while biasing the selection toward areas more likely to fail.

Because the patch-partitioning step uses the observed landslide length–width distribution, the present implementation is best interpreted as a hindcasting and hypothesis-testing workflow. Prospective applications would require an independent landslide size–shape prior, derived from regional inventories, global scaling relationships, or an ensemble of plausible geometric constraints. Finally, in traditional Newmark analyses, the Newmark displacement is usually calculated after identifying unstable areas (Huang et al., 2020; Jibson et al., 2000). However, in this paper, we emphasize the spatial patterns of instability rather than on post-failure deformation magnitudes.

2.4. Simulation Ensemble and Validation Metrics

We evaluate model behavior using an ensemble that spans the regolith-thickness parameterizations described in Section 2.3.2 and a range of cohesion values ($c' = 0$–20 kPa). All other mechanical and seismic parameters are held fixed across runs. Simulations are performed on 30 m grids for each subregion.

Landslide Inventory Data: The observed data set is the coseismic landslide inventory compiled by Roback et al. (2018). The authors mapped over 24,000 coseismic landslides triggered by the Gorkha earthquake and its aftershocks across central Nepal using pre- and post-earthquake high-resolution optical imagery (WorldView-2, -3 and Pleiades), manually delineated at a general ground sample distance of 20–50 cm. The data set is made up of polygonal landslide outlines, classified by failure type and location accuracy. For our analysis, we clipped the inventory to the two subregions used in our model simulations and rasterized the polygons to the 30 m grid resolution of the input DEM. We excluded polygons that were smaller than a single grid cell, since our model is restricted to the pixel resolution of the DEM. The resulting raster layers were used to calculate the magnitude-frequency statistics, along with the spatial distribution of the observed landslides across elevation, slope, and aspect.

Population-Level Comparison Metrics: To quantify the similarity between the modeled and observed landslide distributions, we used two complementary non-parametric statistics: the Kolmogorov–Smirnov (KS)/Kuiper statistic, and the Wasserstein distance. These metrics compare entire probability distributions rather than discrete observations, making them well-suited for evaluating the performance of models designed to reproduce overall distributional characteristics. The KS test quantifies the maximum difference between cumulative distributions and is applied to linear variables (area, elevation, slope), while its circular analog, the Kuiper statistic, is used for topographic aspect (Fisher, 1993). The Wasserstein distance provides a complementary measure of overall distributional offset and is widely used in geomorphology and image-comparison contexts (Rubner et al., 2000). We computed these metrics for four key variables that collectively describe the statistical structure of the landslide population: landslide area, mean elevation, mean slope, and mean aspect. Each of these statistical comparisons was performed on normalized cumulative distributions to eliminate scale effects between variables. These metrics do not evaluate whether individual modeled landslides occur at the same grid cells as mapped landslides and therefore should not be interpreted as measures of pixel-scale predictive skill. Instead, they test whether modeled and mapped landslide populations have similar distributions of size and topographic setting. We therefore interpret them as measures of population-level distributional agreement rather than spatial prediction accuracy.

3. Results

3.1. Influence of Regolith-Thickness Parameterization

We evaluate four primary regolith-thickness parameterizations across both study areas: (a) Uniform 1 m; (b) Inverse-elevation; (c) Curvature-dependent; and (d) Elevation-weighted Curvature. The fifth parameterization, upstream drainage area-dependent, is not shown here due to its intermediate results, largely similar to that of the curvature-based configurations; its implementation is described in Text S1. The spatial organization of representative modeled landslide populations is shown in Figure 5, which compares mapped landslides with model realizations generated using the best-performing model configuration for each subregion. Comparisons for the other regolith-thickness parameterizations are provided for Subregions 1 and 2 in Figures S2 and S3 in Supporting Information S1, respectively. Distributional agreement with the Roback et al. (2018) inventory is assessed using empirical cumulative distribution functions and histograms (Figures 6 and 7) and summarized using Kolmogorov-Smirnov (KS), Kuiper (for aspect), and Wasserstein distances (Figures 8 and 9). As described in Section 2.4, these metrics evaluate population-level agreement in landslide size and topographic setting and are not intended as measures of pixel-scale predictive skill.

3.1.1. Uniform Regolith Thickness

The uniform-depth scenario ($h_s = 1$ m) consistently performed poorest in both subregions. Predicted failures occur widely across slopes and lack the spatial organization seen in the mapped inventory (Figures S2a, S3a in Supporting Information S1). In Subregion 1, this configuration predicts landslides that are generally too large, and at considerably higher elevations than observed in the mapped data set, leading to broad mismatches in elevation,

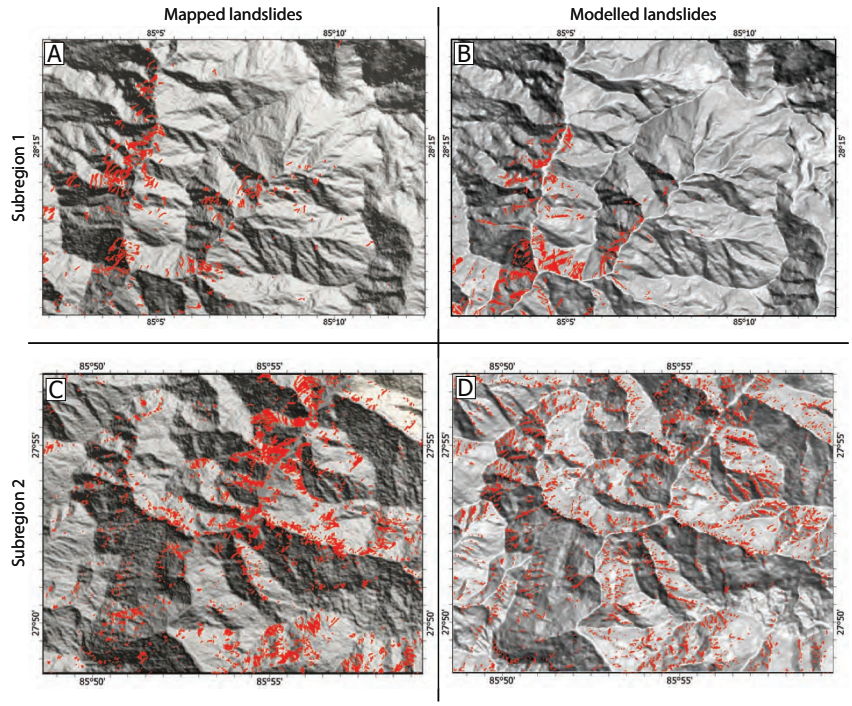


Figure 5. Comparison of mapped and modeled coseismic shallow-landslide populations in the two study subregions. Panels (a and c) show the mapped inventory (Roback et al., 2018); panels (b and d) show representative model realizations generated using the inverse-elevation parameterization (Subregion 1) and the elevation-weighted curvature parameterization (Subregion 2). Landslides are displayed over a 30 m DEM hillshade. The figure illustrates landscape-scale organization of landsliding rather than cell-by-cell spatial agreement.

slope, and area distributions (e.g., area KS $\approx$ 0.40–0.46; slope KS $\approx$ 0.20–0.30), with Wasserstein distances similarly elevated (0.55–0.70), and aspect correspondence weak (Kuiper $\approx$ 0.20–0.27; Figures 6a and 8). A similarly diffuse pattern emerges in Subregion 2, with landslides predicted to be considerably larger than those mapped, with area KS values commonly >0.45 and large Wasserstein distances (0.30–0.70) (Figures 7 and 9). This indicates that a spatially homogeneous regolith field is insufficient to reproduce the observed heterogeneity in either landscape and highlights the importance of introducing spatial organization into regolith-thickness representations.

3.1.2. Inverse-Elevation-Based Regolith Thickness

In Subregion 1, where relief is extremely high and ridgelines are dominated by exposed bedrock, the inverse-elevation based parameterization performs substantially better. Imposing a systematic thinning of regolith with elevation produces a failure pattern concentrated on lower- and mid-slope positions (Figure 5b), closely matching the mapped hypsometric structure. Slope-elevation relations are reproduced most faithfully at cohesion values of approximately 10 kPa, where predicted failures align with the observed concentration of slides on steep, but not extreme, slopes (elevation KS = 0.095, slope KS = 0.084), and corresponding Wasserstein distances (W) = 0.071 (elevation) and 0.104 (slope). Although predicted landslides tend to remain larger than observed (area KS $\approx$ 0.45, $W \approx$ 0.28–0.44), the overall spatial distribution is consistent with a landscape where colluvial material becomes increasingly limited toward high ridges (Figures 6b and 8). In Subregion 2, however, elevation alone does not organize regolith thickness effectively. Area and slope mismatches are moderate to large (e.g., area KS $\approx$ 0.50, $W \approx$ 0.27–0.49; slope KS $\approx$ 0.17–0.26), and aspect correspondence is consistently poorer compared to curvature-modulated approaches (Figures 7b and 9).

3.1.3. Curvature-Based Regolith Thickness

Curvature-based representations of regolith thickness emphasize local convergence and divergence of hillslopes, producing more realistic clustering of unstable terrain, particularly in Subregion 2. In Subregion 1, curvature-only

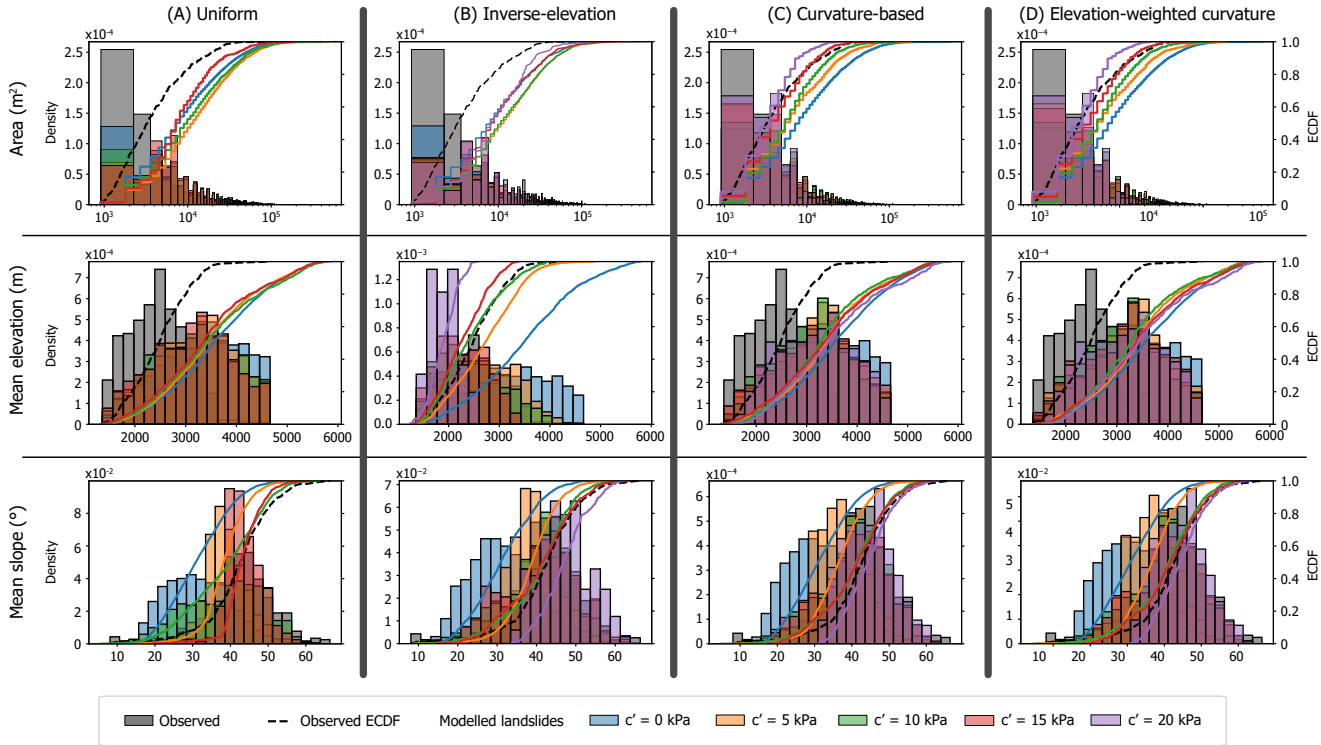


Figure 6. Histograms and empirical cumulative distribution functions (ECDFs) for each model run in Subregion 1. (a) Uniform 1 m regolith depth, (b) Inverse-elevation dependent, (c) Curvature-dependent, (d) Elevation-weighted Curvature-dependent. Gray histograms and dashed black lines show observed landslide distributions; colored curves show results for different cohesion values.

models reproduced area and slope distributions well (area KS $\approx$ 0.11–0.26; slope KS $\approx$ 0.20–0.24), but overpredicted landslides at higher elevations than observed (elevation KS $>$ 0.45). Aspect correspondence was intermediate (Kuiper $\approx$ 0.20–0.23), better than Uniform but weaker than Inverse-elevation (Figures 6 and 8). This suggests that while curvature captures local hillslope structure, curvature-based regolith organization alone is insufficient to reproduce the observed landslide population in this region. However, curvature-only models performed far better in Subregion 2. This landscape contains abundant regolith-mantled hollows and valley-parallel convergent slopes, and the curvature-based parameterization concentrates modeled failures within these features, with predicted landslides having very appropriate sizes (area KS $\approx$ 0.11–0.19), and matching the elevation, slope, and aspect distributions of the mapped landslides extremely well (elevation KS $\approx$ 0.17–0.24, slope KS $\leq$ 0.10, aspect Kuiper $\approx$ 0.20–0.22), all of which are better than any of the purely elevation-based formulations (Figures 7 and 9). Taken together, these results reflect the strong geomorphic influence of planform convergence in shaping landslide patterns, while also showing that it is not always the primary control.

3.1.4. Elevation-Weighted Curvature-based Regolith Thickness

The hybrid parameterization, which couples broad-scale elevation trends with local curvature variability, provides the most balanced representation across both landscapes. In Subregion 1, this approach, combined with $c' =$ 15 kPa improves area (area KS $\approx$ 0.19) and slope (slope KS $=$ 0.089) distributions compared to curvature alone while still reflecting reduced colluvial storage at high elevations. However, similar to the curvature-only parameterization, landslides were still predicted at significantly higher elevations than mapped (elevation KS $\approx$ 0.48), and aspect performance, while moderate (Kuiper $\approx$ 0.20–0.23), did not surpass the Inverse-elevation-based approach (Figures 6c and 8).

In Subregion 2, this combined formulation yields the closest overall match to the mapped population (Figure 5d). It captures the observed pattern of failures concentrated in concave, regolith-rich hollows while still respecting the gentle elevation gradient of this landscape. At $c' =$ 15 kPa, slope preferences, elevation clustering, and aspect organization are all represented with high fidelity (area KS $=$ 0.3, $W =$ 0.165; elevation KS $=$ 0.167,

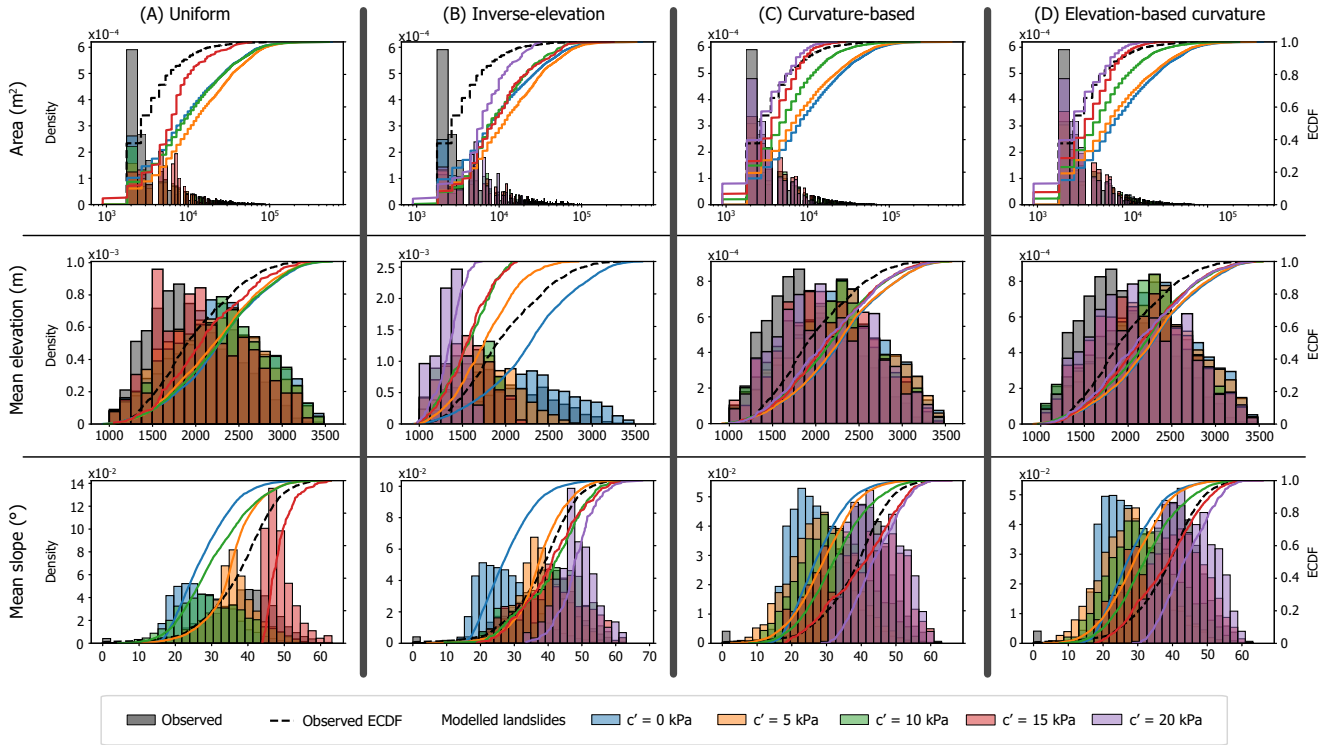


Figure 7. Histograms and empirical cumulative distribution functions (ECDFs) for each model run in Subregion 2. (a) Uniform 1 m regolith depth, (b) Inverse-elevation dependent, (c) Curvature-dependent, (d) Elevation-weighted Curvature-dependent. Gray histograms and dashed black lines show observed landslide distributions; colored curves show results for different cohesion values.

$W = 0.183$; slope KS $= 0.065$, $W = 0.071$; aspect Kuiper $= 0.192$, with a mean aspect deviation of approximately 37°). Taken together, these values make the elevation-weighted curvature configuration the best-performing model for Subregion 2, providing the most coherent multi-metric match to the observed coseismic landslide population (Figures 7c and 9).

3.2. Influence of Cohesion

Across all regolith-thickness parameterizations and in both subregions, model behavior shows a consistent sensitivity to effective cohesion. At low cohesion ($c' = 0$–5 kPa), the model predicts widespread instability, generating unrealistically high numbers of failures across the entire elevation and slope range, with marked increases in both KS and Wasserstein distances. At high cohesion ($c' \approx 20$ kPa), instability is strongly suppressed, yielding too few failures compared to the inventory. This pattern emerges in both subregions (e.g., Subregion 1: elevation KS $= 0.095$ at $c' = 15$ kPa vs. ≥ 0.45 for $c' = 0$ kPa; Subregion 2: slope KS $= 0.065$ at $c' = 15$ kPa vs. KS $= 0.183$–0.246 at $c' = 0$–5 kPa).

Intermediate cohesion values of $c' \approx$ 10–15 kPa produce the closest distributional agreement with the mapped landslide populations (Figures 6 and 7). This narrow optimal range is consistent with cohesion values typically associated with shallow, regolith-sourced failures (Montgomery & Dietrich, 1994) and supports the sensitivity of the model to realistic strength values.

3.3. Subregional Contrasts

The ensemble reveals consistent but contrasting controls on coseismic landsliding in the two landscapes. In Subregion 1, the Inverse-elevation parameterization provides the closest match to the mapped population across elevation, slope, and aspect, with curvature-based models performing less well, particularly for elevation distributions (Figures 6 and 8). In contrast, in Subregion 2, curvature-informed parameterizations, especially the Elevation-weighted Curvature model, produce the lowest KS and Wasserstein distances for area, elevation, and slope, along with the strongest correspondence in aspect (Figures 7c and 9).

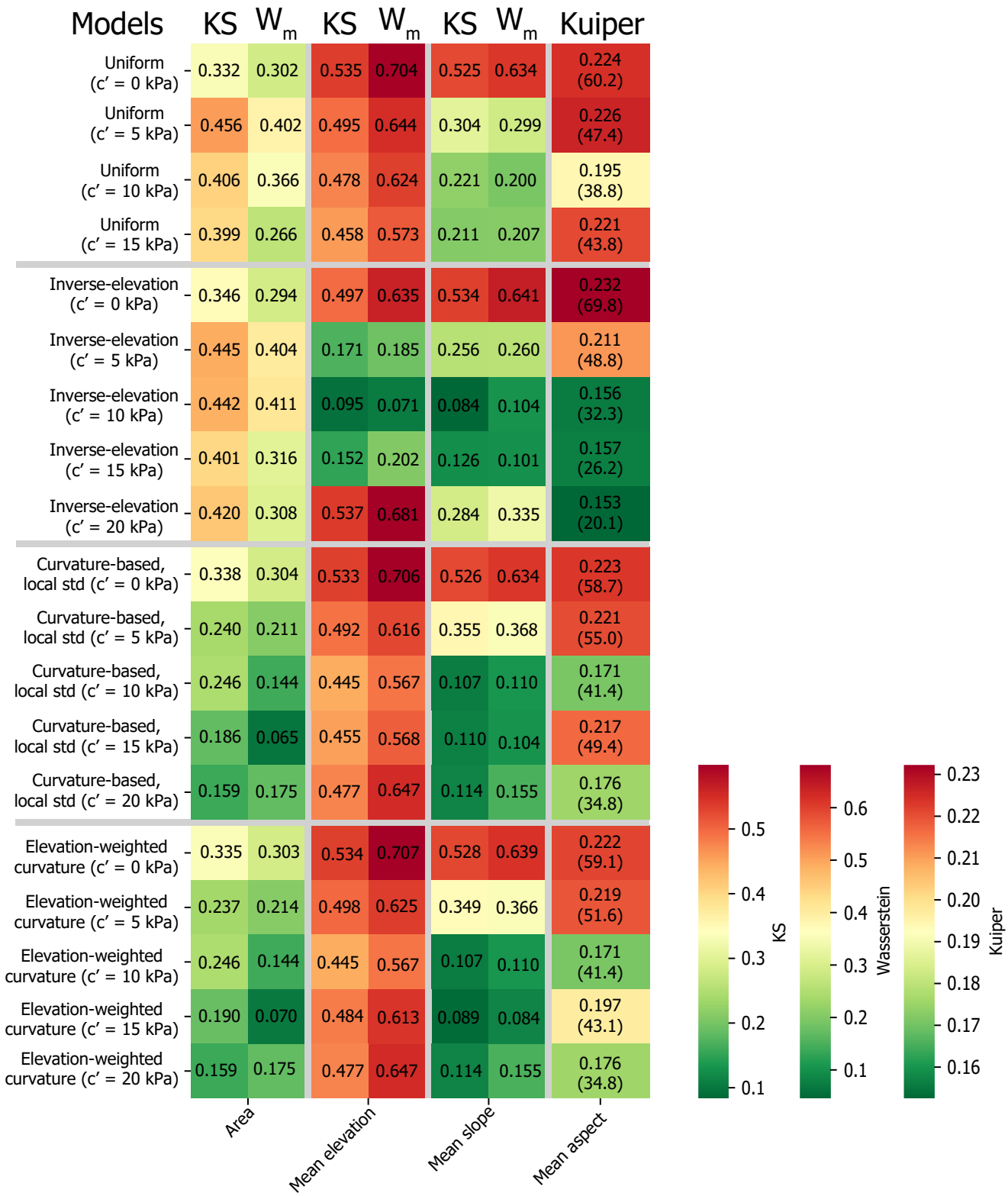


Figure 8. Model performance heatmaps for subregion 1, comparing modeled and observed distributions of landslide area, elevation, slope, and aspect. Colors show Kolmogorov–Smirnov and Wasserstein distances for linear variables and the Kuiper statistic for aspect. Values are shown for all regolith-thickness parameterizations and cohesion values.

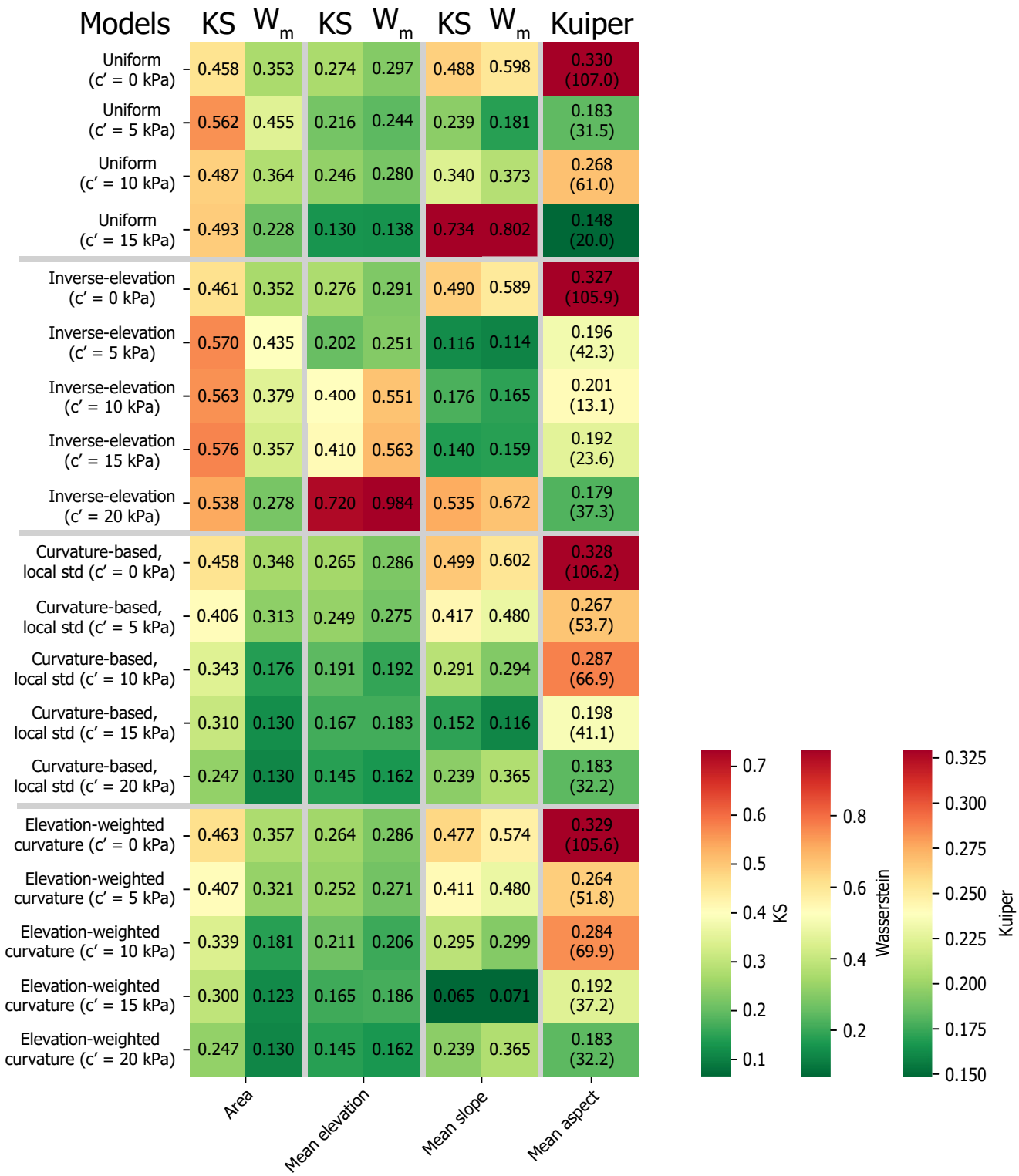


Figure 9. Model performance heatmaps for subregion 2, comparing modeled and observed distributions of landslide area, elevation, slope, and aspect. Colors show Kolmogorov–Smirnov and Wasserstein distances for linear variables and the Kuiper statistic for aspect. Values are shown for all regolith-thickness parameterizations and cohesion values.

Across the full ensemble, these results show that the dominant regolith-organization hypotheses differ between the landscapes. Subregion 1 is reproduced most successfully by parameterizations emphasizing large-scale elevation structure, whereas Subregion 2 aligns most closely with models incorporating curvature-driven local variability. Although the optimal cohesion range is similar across both subregions (Section 3.2), the performance of each regolith-thickness parameterization remains landscape-specific. These contrasts identify the regolith-organization hypotheses that are most consistent with the observed landslide populations within the tested model framework, rather than uniquely determining the true distribution of regolith thickness.

4. Discussion

The model ensemble demonstrates that the population-level characteristics of coseismic shallow landsliding are strongly sensitive to the spatial organization of regolith thickness. Parameterizations incorporating elevation-dependent thinning, curvature-informed convergence, or both consistently outperform the spatially uniform baseline, although the best-performing form of regolith organization differs between the two study landscapes. These contrasts indicate that mapped landslide populations contain information that can be used to evaluate competing hypotheses of landscape-scale regolith organization.

The Gorkha earthquake is used here as a natural test case for posing broader geomorphic questions about how regolith organization influences coseismic shallow-landslide populations. The experiments are not intended to reproduce every landslide triggered by the earthquake, recover a unique map of regolith thickness, or predict individual failure locations. Instead, they compare the population-level consequences of alternative regolith-thickness hypotheses within a common physical–statistical framework. The distributions of landslide area, elevation, slope, and aspect do not measure cell-by-cell spatial accuracy, but they describe the sizes and topographic settings occupied by the modeled and mapped populations. They therefore provide a meaningful basis for evaluating how alternative representations of regolith organization affect landscape-scale landslide response.

Model performance is also sensitive to effective cohesion. Moderate effective cohesions ($c' \approx$ 10–15 kPa) yield the closest overall agreement with the mapped inventories in both subregions, whereas lower values produce widespread instability and higher values suppress failure. However, changing cohesion does not reproduce the systematic and contrasting responses to regolith organization observed between the two landscapes. The following sections consider the geomorphic interpretation of these contrasts, the evidence that the model captures the widespread shallow-failure component of the Gorkha inventory, and the limitations affecting interpretation of the experiments.

4.1. Contrasting Regolith Thickness Distributions Between Subregions

The differing performance of the regolith-thickness parameterizations demonstrates that topography regulates both the scale and the structure of regolith accumulation, and that this organization strongly influences coseismic shallow-failure patterns. The model ensemble reveals contrasting controls on landslide occurrence in the two subregions. In Subregion 1, the Inverse-elevation parameterization provides the closest correspondence across slope, elevation, and aspect, suggesting that broad hypsometric trends, particularly thinning of regolith toward higher ridges, play a primary role in shaping coseismic failure patterns (Figure 5b). In contrast, Subregion 2 is reproduced most successfully by curvature-informed parameterizations, particularly when combined with a modest elevation weighting, indicating that local topographic convergence exerts a stronger influence on regolith organization and landslide clustering than broad elevation gradients (Figure 5d).

Several alternative explanations for these contrasting outcomes can be evaluated using the model ensemble. One possibility is that uncertainties in shallow-failure mechanics limit the ability of the model to reproduce observed landslide patterns. However, a narrow and physically realistic cohesion range yields the closest agreement in both landscapes, indicating that the underlying mechanics operate consistently and are unlikely to explain the differing model behavior. A second possibility is that limitations associated with DEM resolution or model resolution generate the observed discrepancies. If this were the primary control, all parameterizations would be expected to perform similarly across both subregions because identical input data, preprocessing procedures, and modeling workflows were used throughout. Instead, the ensemble exhibits systematic differences, and in some cases reversals, in model performance between regolith-thickness parameterizations. Lithology may also exert an influence on regolith production and material properties. However, both subregions lie within the High Himalaya and are underlain by rock units of broadly similar composition (Dhital, 2015). The optimal cohesion range is also

nearly identical between the two regions, and model performance aligns more closely with the imposed organization of regolith thickness than with mapped lithological boundaries. Together, these observations suggest that the contrasting model behavior is most plausibly explained by differences in landscape form and the spatial organization of near-surface materials.

These contrasting responses are consistent with a transition in the dominant controls on regolith organization associated with differences in soil-mantle continuity. Recent work has highlighted how landscapes evolve from continuously soil-mantled hillslopes toward patchy regolith cover and ultimately bedrock-dominated terrain as relief increases and erosion outpaces regolith production (Heimsath et al., 2012; Rossi et al., 2026). In such settings, topographically mediated transport processes may no longer provide a complete description of regolith distribution, and rock strength, erosion rates, and patchy soil cover become increasingly important (Geyman et al., 2025).

Subregion 2 is characterized by rolling, regolith-mantled terrain and lower overall relief (2712 m; Figure 2). Curvature-based parameterizations perform best in this landscape, consistent with hillslope-evolution theory that predicts preferential accumulation of colluvium in convergent hollows and thinning on convex slopes (Dietrich et al., 1995; Heimsath et al., 1997; Roering, 2008). Their success reflects the abundance of convergent hillslopes and shallow colluvial stores within this landscape (Clubb et al., 2016; Gabet et al., 2021; Hurst et al., 2012). In contrast, Subregion 1 exhibits extensive exposed bedrock, steep ridgelines, and substantially greater relief (4,626 m; Figure 2). Here, curvature alone does not capture the dominant control on regolith thickness, and landslide populations are reproduced more effectively when regolith thins systematically with elevation. These results suggest that broad hypsometric structure, rather than local topographic convergence, exerts the primary control on regolith availability and hence the spatial distribution of coseismic failures.

This behavior is consistent with observations from other tectonically active mountain belts, including the San Gabriel Mountains, where hillslope form reflects a balance between large-scale relief organization and local convergence in threshold landscapes (DiBiase et al., 2012). Taken together, these comparisons reinforce the idea that the scale and style of topographic organization determine whether hypsometry or curvature exerts the dominant influence on regolith thickness in steep terrain. An important implication of the ensemble is that curvature-based parameterizations should not be assumed to apply universally. Curvature performs best in landscapes characterized by well-developed convergent hollows and an extensive regolith mantle, whereas elevation-dependent formulations appear more appropriate where regolith is patchy and bedrock exposure is widespread. The most appropriate representation of regolith thickness is therefore likely to be landscape dependent.

More broadly, these results demonstrate that hybrid physical–statistical approaches can be used to evaluate process-based hypotheses regarding regolith architecture and its influence on coseismic susceptibility. They extend the growing use of physically based distributed stability models that seek to represent not only landslide susceptibility, but also the size and organization of landslide populations (Bellugi et al., 2015; Milledge et al., 2014). In this context, landslide inventories become not only a record of coseismic response, but also a means of testing competing hypotheses about the organization of near-surface materials in mountainous landscapes where direct observations remain sparse.

4.2. Evidence for Shallow Coseismic Landsliding

Multiple lines of evidence from the model ensemble, considered alongside established observations of the 2015 Gorkha earthquake, support the interpretation that the framework captures the widespread shallow, regolith-sourced component of coseismic landsliding. First, the effective cohesion range that provides the closest agreement with the mapped inventory is consistently $c' \approx$ 10–15 kPa across the regolith-thickness parameterizations and in both subregions. These values are characteristic of loose colluvium and mobile regolith rather than saprolite or bedrock (Cho & Lee, 2002; Wong & Ho, 2000). The strong overprediction of failures at very low cohesion and suppression of failures at high cohesion support the interpretation that the mapped population is dominated by failures occupying a mechanical window typical of shallow sliding surfaces.

Second, parameterizations that incorporate spatial variability in regolith thickness consistently outperform the uniform-thickness baseline, indicating that the organization of near-surface material exerts a first-order control on the reproduced landslide population (Parker et al., 2016). This behavior is consistent with the interpretation that failures preferentially occur where topographically organized regolith overlies steep hillslopes. The uniform-depth model provides a useful experimental contrast because it retains the same stability framework and

characteristic regolith thickness while removing the spatial organization represented by the alternative parameterizations. Third, the mapped Gorkha landslides themselves exhibit characteristics typical of shallow translational failures. They are generally small to moderate in area, concentrated in concave hollows and mid-to lower-hillslope positions, and show strong dependence on local slope and aspect (Roback et al., 2018). The enhanced model sensitivity to curvature in Subregion 2 further reinforces the importance of near-surface material organization in controlling landslide occurrence.

Taken together, the consistency between the preferred effective cohesion range, the improved performance of spatially organized regolith-thickness parameterizations, and the observed topographic characteristics of the Gorkha inventory supports the interpretation that the framework captures the widespread shallow, regolith-sourced component of coseismic landsliding. The presence of other failure mechanisms within the inventory does not negate this correspondence, although it contributes to the residual disagreement between the modeled and mapped populations, as considered below.

4.3. Limitations of the Model Experiments

The mapped inventory has limitations relevant to the model comparison. Post-event mapping may be less complete in sparsely vegetated alpine terrain, potentially contributing to the mismatch at high elevations in Subregion 1 (Harvey et al., 2024). However, Roback et al. (2018) also show that landslide density follows earthquake source characteristics and rupture geometry, placing higher densities away from some of the highest ridges. Inventory incompleteness is therefore one of several possible contributors to the residual mismatch rather than a sufficient explanation for the observed elevation distribution. In addition, although shallow failures formed a widespread component of the Gorkha landslide population, the earthquake also triggered a smaller number of bedrock landslides, large rock avalanches, and deep-seated failures (Kargel et al., 2015; Meena & Tavakkoli Piralilou, 2019). These failure types are influenced by structural discontinuities, lithological contrasts, and deeper mechanical conditions outside the scope of the shallow-regolith formulation (Campforts et al., 2022). Their presence contributes to residual disagreement, particularly in the upper tail of the landslide-area distributions, but does not prevent population-level evaluation of the widespread shallow-failure component represented by the model.

The regolith-thickness parameterizations are simplified, geomorphically informed hypotheses rather than independently validated maps of subsurface thickness. The uniform 1 m configuration is an experimental baseline that removes spatial variability and is not intended as a realistic description of steep Himalayan terrain. Its comparison with the spatially variable parameterizations tests whether introducing landscape-scale organization improves the reproduced landslide populations under otherwise consistent conditions. The results therefore identify which of the tested hypotheses are most consistent with the inventory rather than uniquely determining the true regolith-thickness field. Similarly, $c' = 10$–15 kPa represents an effective cohesion range within the model. Its consistent performance across the two subregions and agreement with published values for shallow colluvium support its physical plausibility, although it is not a direct measurement of regional material strength.

Uncertainty also remains in the hydrological and seismic forcing. Saturation and friction angle are held constant to isolate the effects of regolith-thickness organization and cohesion, although these properties vary spatially in natural landscapes. The USGS ShakeMap provides a common spatially distributed forcing field for all experiments, but does not resolve all uncertainty associated with interpolation, local site effects, topographic amplification, rupture directivity, or the full acceleration history. In addition, the critical-acceleration formulation does not represent shaking duration, frequency content, or post-initiation displacement. These simplifications may contribute to residual mismatch and limit reconstruction of the complete Gorkha event. However, because every regolith-thickness parameterization is evaluated using the same forcing, material assumptions, DEM processing, and population-realization procedure, systematic differences among the experiments remain informative for comparing the competing regolith-organization hypotheses.

Finally, the 30 m DEM and population-realization procedure define the spatial scale of the analysis. DEM smoothing cannot represent narrow hollows, road cuts, or sharp bedrock structures below the grid scale, while the partitioning and stochastic sampling procedures generate plausible landslide populations rather than exact failure footprints. These limitations identify priorities for future testing using more detailed inventory classifications, direct regolith observations, and ensembles of hydrological and seismic forcing. Within the present controlled experiments, however, the results robustly show that alternative forms of regolith organization generate systematic, landscape-specific differences in coseismic shallow-landslide populations.

5. Conclusions

In this study, we introduced *ShallowLandslider*, a hybrid physical–statistical framework that combines critical-acceleration slope-stability calculations with stochastic realization of landslide populations. The model provides a means of evaluating competing regolith-organization hypotheses using mapped coseismic landslide inventories. Across two geomorphically contrasting landscapes affected by the 2015 Gorkha earthquake, parameterizations that incorporate spatial organization of regolith thickness consistently outperform a spatially uniform baseline. The results demonstrate that reproducing the observed distributions of landslide area, elevation, slope, and aspect requires representation of landscape-scale variability in regolith thickness. Within the range of material properties explored here, model performance is more sensitive to the imposed organization of regolith thickness than to variations in cohesion alone.

The two study areas favor contrasting regolith-organization hypotheses: In the high-relief, bedrock-dominated terrain of Subregion 1, parameterizations incorporating broad elevation-dependent thinning provide the closest overall agreement with the mapped landslide population, although curvature-informed parameterizations reproduce landslide magnitude-frequency distributions particularly well. In the lower-relief, more extensively regolith-mantled terrain of Subregion 2, curvature-informed parameterizations that capture local topographic convergence provide the strongest distributional agreement. These contrasting outcomes suggest that the most appropriate representation of regolith architecture depends on landscape form and degree of soil mantling. Across both subregions, the closest agreement between modeled and mapped landslide populations occurs for moderate cohesion values ($c' \approx$ 10–15 kPa), consistent with shallow, regolith-sourced failures. However, the results do not uniquely determine the true distribution of regolith thickness, nor do they exclude additional influences arising from uncertainty in the shaking field, site effects, groundwater conditions, material heterogeneity, or inventory limitations. Instead, they identify the regolith-organization hypotheses that are most consistent with the observed landslide populations within the tested model framework.

Taken together, these results demonstrate that hybrid physical–statistical models can be used not only to simulate coseismic shallow-landslide populations, but also to evaluate competing hypotheses about regolith organization in landscapes where direct observations remain sparse. More broadly, the study highlights the importance of coupling physically based slope-stability modeling with realistic representations of regolith architecture when seeking to understand the landscape-scale organization of coseismic shallow landsliding.

Conflict of Interest

The authors declare no conflicts of interest relevant to this study.

Availability Statement

ShallowLandslider is implemented in `Python 3.12`, building on the open-source Landlab library (Barnhart et al., 2020; Hobley et al., 2017). Core dependencies include `NumPy`, `Pandas`, `SciPy`, and `Matplotlib` for numerical computation and visualization. All model parameters, file paths, and runtime options are defined in a structured `YAML` configuration file, facilitating reproducible simulations and parameter sweeps. The code is under active development and is freely available through GitHub (https://github.com/thermok-SG/EQShallowLandslider). The version used in this study is permanently archived on Zenodo (Ghoshal et al., 2026).

Acknowledgments
The authors thank the Community Surface Dynamics Modeling System (CSDMS) for developing and maintaining the Landlab modeling framework used in this study. We also acknowledge OpenTopography for providing access to the DEM data. This research was supported by a NERC Pushing the Frontiers Grant to SB (NE/Y000080/1).

References

Avouac, J.-P. P., Meng, L., Wei, S., Wang, T., & Ampuero, J. P. (2015). Lower edge of locked main Himalayan thrust unzipped by the 2015 Gorkha earthquake. *Nature Geoscience*, *8*(9), 708–711. https://doi.org/10.1038/ngeo2518

Barnhart, K. R., Hutton, E. W., Tucker, G. E., Gasparini, N. M., Istanbulluoglu, E., Hobley, D. E. J., et al. (2020). Short communication: Landlab v2.0: A software package for Earth surface dynamics. *Earth Surface Dynamics*, *8*(2), 379–397. https://doi.org/10.5194/esurf-8-379-2020

Bellugi, D., Milledge, D. G., Dietrich, W. E., McKean, J. A., Perron, J. T., Sudderth, E. B., & Kazian, B. (2015). A spectral clustering search algorithm for predicting shallow landslide size and location. *Journal of Geophysical Research: Earth Surface*, *120*(2), 300–324. https://doi.org/10.1002/2014JF003137

Campforts, B., Shobe, C. M., Overeem, I., & Tucker, G. E. (2022). The art of landslides: How stochastic mass wasting shapes topography and influences landscape dynamics. *Journal of Geophysical Research: Earth Surface*, *127*(8), e2022JF006745. https://doi.org/10.1029/2022JF006745

Catani, F., Segoni, S., & Falorni, G. (2010). An empirical geomorphology-based approach to the spatial prediction of soil thickness at catchment scale. *Water Resources Research*, *46*(5). https://doi.org/10.1029/2008WR007450

Cho, S., & Lee, S. (2002). Evaluation of surficial stability for homogeneous slopes considering rainfall characteristics. *Journal of Geotechnical and Geoenvironmental Engineering*, *128*(9), 756–763. https://doi.org/10.1061/(ASCE)1090-0241(2002)128:9(756)

Claessens, L., Schoorl, J. M., & Veldkamp, A. (2007). Modelling the location of shallow landslides and their effects on landscape dynamics in large watersheds: An application for Northern New Zealand. *Geomorphology*, *87*(1), 16–27. https://doi.org/10.1016/j.geomorph.2006.06.039

Clubb, F. J., Mudd, S. M., Attal, M., Milodowski, D. T., & Grieve, S. W. (2016). The relationship between drainage density, erosion rate, and hilltop curvature: Implications for sediment transport processes. *Journal of Geophysical Research: Earth Surface*, *121*(10), 1724–1745. https://doi.org/10.1002/2015JF003747

Crozier, M. J., Vaughan, E. E., & Tippett, J. M. (1990). Relative instability of colluvium-filled bedrock depressions. *Earth Surface Processes and Landforms*, *15*(4), 329–339. https://doi.org/10.1002/esp.3290150404

Dhital, M. R. (2015). Geology of the Nepal Himalaya: Regional perspective of the classic collided orogen. *Geology of the Nepal Himalaya: Regional Perspective of the Classic Collided Orogen*, 1–498. https://doi.org/10.1007/978-3-319-02496-7

DiBiase, R. A., Heimsath, A. M., & Whipple, K. X. (2012). Hillslope response to tectonic forcing in threshold landscapes. *Earth Surface Processes and Landforms*, *37*(8), 855–865. https://doi.org/10.1002/esp.3205

DiBiase, R. A., Whipple, K. X., Heimsath, A. M., & Ouimet, W. B. (2010). Landscape form and millennial erosion rates in the San Gabriel Mountains, CA. *Earth and Planetary Science Letters*, *289*(1–2), 134–144. https://doi.org/10.1016/j.epsl.2009.10.036

Dietrich, W. E., Bellugi, D. G., Sklar, L. S., Stock, J. D., Heimsath, A. M., & Roering, J. J. (2013). Geomorphic transport laws for predicting landscape form and dynamics. In P. R. Wilcock & R. M. Iverson (Eds.), *Geophysical monograph series* (pp. 103–132). American Geophysical Union. https://doi.org/10.1029/135GM09

Dietrich, W. E., Reiss, R., Hsu, M.-L., & Montgomery, D. R. (1995). A process-based model for colluvial soil depth and shallow landsliding using digital elevation data. *Hydrological Processes*, *9*(3–4), 383–400. https://doi.org/10.1002/hyp.3360090311

D'Odorico, P., & Fagherazzi, S. (2003). A probabilistic model of rainfall-triggered shallow landslides in hollows: A long-term analysis. *Water Resources Research*, *39*(9), 2002WR001595. https://doi.org/10.1029/2002WR001595

Fan, X., Scaringi, G., Korup, O., West, A. J., Van Westen, C. J., Tanyas, H., et al. (2019). Earthquake-induced chains of geologic hazards: Patterns, mechanisms, and impacts. *Reviews of Geophysics*, *57*(2), 421–503. https://doi.org/10.1029/2018RG000626

Fisher, N. I. (1993). *Statistical analysis of circular data* (1st ed.). Cambridge University Press. https://doi.org/10.1017/CBO9780511564345

Gabet, E. J., Mudd, S. M., Wood, R. W., Grieve, S. W. D., Binnie, S. A., & Dunai, T. J. (2021). Hilltop curvature increases with the square root of erosion rate. *Journal of Geophysical Research: Earth Surface*, *126*(5), e2020JF005858. https://doi.org/10.1029/2020JF005858

Geyman, E. C., Paige, D. A., & Lamb, M. P. (2025). The contribution of rock strength to soil production. *Nature*, *647*(8091), 921–927. https://doi.org/10.1038/s41586-025-09751-z

Ghoshal, S., Boulton, S., Hales, T. C., & Campforts, B. (2026). ShallowLandslider v1.0 [Software]. Retrieved from https://doi.org/10.5281/zenodo.21337764

Harvey, E. L., Kincey, M. E., Rosser, N. J., Gadtaula, A., Collins, E., Densmore, A. L., et al. (2024). Review of landslide inventories for Nepal between 2010 and 2021 reveals data gaps in global landslide hotspot. *Natural Hazards*, *121*(5), 5075–5101. https://doi.org/10.1007/s11069-024-07013-1

Heimsath, A. M., DiBiase, R. A., & Whipple, K. X. (2012). Soil production limits and the transition to bedrock-dominated landscapes. *Nature Geoscience*, *5*(3), 210–214. https://doi.org/10.1038/ngeo1380

Heimsath, A. M., Dietrich, W. E., Nishiizumi, K., & Finkel, R. C. (1997). The soil production function and landscape equilibrium. *Nature*, *388*(6640), 358–361. https://doi.org/10.1038/41056

Hobley, D. E., Adams, J. M., Siddhartha Nudurupati, S., Hutton, E. W., Gasparini, N. M., Istanbulluoglu, E., & Tucker, G. E. (2017). Creative computing with Landlab: An open-source toolkit for building, coupling, and exploring two-dimensional numerical models of Earth-surface dynamics. *Earth Surface Dynamics*, *5*(1), 21–46. https://doi.org/10.5194/esurf-5-21-2017

Hovius, N., Meunier, P., Lin, C.-W., Chen, H., Chen, Y.-G., Dadson, S., et al. (2011). Prolonged seismically induced erosion and the mass balance of a large earthquake. *Earth and Planetary Science Letters*, *304*(3–4), 347–355. https://doi.org/10.1016/j.epsl.2011.02.005

Huang, D., Wang, G., Du, C., Jin, F., Feng, K., & Chen, Z. (2020). An integrated SEM-Newmark model for physics-based regional coseismic landslide assessment. *Soil Dynamics and Earthquake Engineering*, *132*, 106066. https://doi.org/10.1016/j.soildyn.2020.106066

Hurst, M. D., Mudd, S. M., Walcott, R., Attal, M., & Yoo, K. (2012). Using hilltop curvature to derive the spatial distribution of erosion rates. *Journal of Geophysical Research*, *117*(F2). https://doi.org/10.1029/2011JF002057

Jibson, R. W., Harp, E. L., & Michael, J. A. (2000). A method for producing digital probabilistic seismic landslide hazard maps. *Engineering Geology*, *58*(3–4), 271–289. https://doi.org/10.1016/S0013-7952(00)00039-9

Kargel, J. S., Leonard, G. J., Shugar, D. H., Haritashya, U. K., Bevington, A., Fielding, E. J., et al. (2015). Geomorphic and geologic controls of geohazards induced by Nepal's 2015 Gorkha earthquake. *Science*, *351*(6269), aac8353. https://doi.org/10.1126/science.aac8353

Kritikos, T., Robinson, T. R., & Davies, T. R. H. (2015). Regional coseismic landslide hazard assessment without historical landslide inventories: A new approach. *Journal of Geophysical Research: Earth Surface*, *120*(4), 711–729. https://doi.org/10.1002/2014JF003224

Li, A., Tan, X., Wu, W., Liu, H., & Zhu, J. (2017). Predicting active-layer soil thickness using topographic variables at a small watershed scale. *PLoS One*, *12*(9), e0183742. https://doi.org/10.1371/journal.pone.0183742

Meena, S. R., & Tavakkoli Piralilou, S. (2019). Comparison of earthquake-triggered landslide inventories: A case study of the 2015 gorkha earthquake, Nepal. *Geosciences*, *9*(10), 437. https://doi.org/10.3390/geosciences9100437

Milledge, D. G., Bellugi, D., McKean, J. A., Densmore, A. L., & Dietrich, W. E. (2014). A multidimensional stability model for predicting shallow landslide size and shape across landscapes. *Journal of Geophysical Research: Earth Surface*, *119*(11), 2481–2504. https://doi.org/10.1002/2014JF003135

Montgomery, D. R., & Dietrich, W. E. (1994). A physically based model for the topographic control on shallow landsliding. *Water Resources Research*, *30*(4), 1153–1171. https://doi.org/10.1029/93WR02979

Newmark, N. M. (1965). Effects of earthquakes on dams and embankments. *Géotechnique*, *15*(2), 139–160. https://doi.org/10.1680/geot.1965.15.2.139

Pack, R., Tarboton, D., & Goodwin, C. (1998). The SINMAP approach to terrain stability mapping. In *Proceedings of the 8th congress of the international association of engineering geology* (Vol. 2). Engineering Geology and Natural Hazards).

Park, S. J., McSweeney, K., & Lowery, B. (2001). Identification of the spatial distribution of soils using a process-based terrain characterization. *Geoderma*, *103*(3), 249–272. https://doi.org/10.1016/S0016-7061(01)00042-8

Parker, R. N., Hales, T. C., Mudd, S. M., Grieve, S. W. D., & Constantine, J. A. (2016). Colluvium supply in humid regions limits the frequency of storm-triggered landslides. *Scientific Reports*, *6*(1), 34438. https://doi.org/10.1038/srep34438

Parker, R. N., Hancox, G. T., Petley, D. N., Massey, C. I., Densmore, A. L., & Rosser, N. J. (2015). Spatial distributions of earthquake-induced landslides and hillslope preconditioning in the northwest South Island, New Zealand. *Earth Surface Dynamics*, *3*(4), 501–525. https://doi.org/10.5194/esurf-3-501-2015

Patton, N. R., Lohse, K. A., Godsey, S. E., Crosby, B. T., & Seyfried, M. S. (2018). Predicting soil thickness on soil mantled hillslopes. *Nature Communications*, *9*(1), 3329. https://doi.org/10.1038/s41467-018-05743-y

Pelletier, J. D., & Rasmussen, C. (2009). Geomorphically based predictive mapping of soil thickness in upland watersheds. *Water Resources Research*, *45*(9). https://doi.org/10.1029/2008WR007319

Petley, D. (2012). Global patterns of loss of life from landslides. *Geology*, *40*(10), 927–930. https://doi.org/10.1130/G33217.1

Roback, K., Clark, M. K., West, A. J., Zekkos, D., Li, G., Gallen, S. F., et al. (2018). The size, distribution, and mobility of landslides caused by the 2015 Mw7.8 Gorkha earthquake, Nepal. *Geomorphology*, *301*, 121–138. https://doi.org/10.1016/j.geomorph.2017.01.030

Roering, J. J. (2008). How well can hillslope evolution models "explain" topography? Simulating soil transport and production with high-resolution topographic data. *GSA Bulletin*, *120*(9–10), 1248–1262. https://doi.org/10.1130/B26283.1

Rossi, M. W., Tucker, G. E., Anderson, S. P., Anderson, R. S., & McGlinchy, J. (2026). Coevolving topography, patchy soils, and forest structure. *Proceedings of the National Academy of Sciences*, *123*(12), e2519374123. https://doi.org/10.1073/pnas.2519374123

Rubner, Y., Tomasi, C., & Guibas, L. J. (2000). The Earth Mover's distance as a metric for image retrieval. *International Journal of Computer Vision*, *40*(2), 99–121. https://doi.org/10.1023/A:1026543900054

Segoni, S., Rossi, G., & Catani, F. (2012). Improving basin scale shallow landslide modelling using reliable soil thickness maps. *Natural Hazards*, *61*(1), 85–101. https://doi.org/10.1007/s11069-011-9770-3

USGS. (2015). M 7.8 - 67 km NNE of Bharatpur, Nepal. Retrieved from https://earthquake.usgs.gov/earthquakes/eventpage/us20002926

Wang, J., Howarth, J. D., McClymont, E. L., Densmore, A. L., Fitzsimons, S. J., Croissant, T., et al. (2020). Long-term patterns of hillslope erosion by earthquake-induced landslides shape mountain landscapes. *Science Advances*, *6*(23), eaaz6446. https://doi.org/10.1126/sciadv.aaz6446

Wong, H., & Ho, K. (2000). Preliminary quantitative risk assessment of earthquake-induced landslides at man-made slopes in Hong Kong. (Tech. Rep. No. GEO Report No. 98). *Hong Kong SAR: Civil Engineering Department: Geotechnical Engineering Office*.

Zevenbergen, L. W., & Thorne, C. R. (1987). Quantitative analysis of land surface topography. *Earth Surface Processes and Landforms*, *12*(1), 47–56. https://doi.org/10.1002/esp.3290120107